Coastal Engineering 173 (2022) 104093

Contents lists available at ScienceDirect

Coastal Engineering

journal homepage: www.elsevier.com/locate/coastaleng

Bridge-piling modifications on tidal flows in an estuary

Carmen Zarzuelo [a,*], Alejandro López-Ruiz [a], Arnoldo Valle-Levinson [b], Manuel Díez-Minguito [c], Miguel Ortega-Sánchez [c]

[a] Departamento de Ingeniería Aeroespacial y Mecánica de Fluidos, Universidad de Sevilla, Camino de los Descubrimientos s/n, 41092, Seville, Spain
[b] Department of Civil and Coastal Engineering, University of Florida, 365 Weil Hall, P.O. Box 116580, Gainesville, FL 32611, USA
[c] Andalusian Institute for Earth System Research, University of Granada, Avda. del Mediterráneo, s/n, 18006 Granada, Spain

ARTICLE INFO

Keywords:
Bridge-pile
Tidal flow
Field survey
Numerical modeling
Estuary

ABSTRACT

This paper investigates the impact of the bridge-pilling modifications on the tidal flow at the strait of a human-altered mesotidal estuary (Cádiz Bay, Spain). The analysis was accomplished by combining (1) field data of current velocities in a cross-section close to the pile of a recently built bridge, and (2) hydrodynamics results from the calibrated and tested DELFT3D numerical model on the study site. The analysis was focused on bridge piling effects at intratidal scale during neap and spring tides. Semidiurnal (D2), quarti-diurnal (D4) and sixth-diurnal (D6) bands were examined. The ratio of quarter-diurnal to semidiurnal amplitudes (D4/D2) is largest (>1) near the bottom of the channel due to friction, and the ratio D6/D2 is largest (>1.5) close to the pile and in the shallowest part of the cross-section, due to internal asymmetry and tidal advective accelerations. Comparing neap and spring tides, the most marked asymmetries are found in the latter. These asymmetries occur around the wake of the pile, alternating from flood to ebb. The location of the bridge pile causes a decrease in the amplitude of D2 (50%), and a phase lag in the tidal wave of 30 min. The D6 amplitude increases up to almost 100% due to distortion of the tidal wave induce by the wake created at the pile. Moreover, the pile reduces about 1 m the depth where the pycnocline is observed. Additionally, the pile can be considered as an obstacle for the sediment flux. These effects can be extrapolated to similar infrastructures, such as wind or wave energy farms, that can potentially modify the estuarine dynamics.

1. Introduction

Estuarine environments evolved rapidly during the Holocene transgression and their complexity was shaped by diverse interactions among hydrodynamics, geomorphology, biogeochemical processes, climate variability, and human interventions. General patterns of the behavior of estuaries can be derived through the analysis of observations (Geyer and MacCready, 2014; Valle-Levinson, 2021; Murshid and Mariotti, 2021) that also respond to human activities like dams or bridges (Wu et al., 2016; Andersen et al., 2020; Guo et al., 2020).

Studies have also assessed the resilience or adaptation time of estuaries to human interventions (Dastgheib et al., 2008; Wang et al., 2018). Wei et al. (2017) analyzed the influence of river damming on shoal morphodynamics. The effects of channel deepening in Delaware Bay (USA) were analyzed by Pareja-Roman et al. (2020), who studied modifications on tidal range, sediment transport, and pollutant dispersal. Cearreta et al. (2004) studied how human exploitation of marshes can affect biological processes due to changes of the dynamics.

The piles that support bridges may also alter tidal wave propagation on the near-field, thereby modifying the local hydrodynamics and sediment transport. The effects of bridge piles have been widely studied in fluvial dynamics (e.g., Chen et al. (2013), Wang et al. (2018)) or only as an experimental study on scour at complex bridge piers exposed to combined waves and currents (Yang et al., 2020), although the number of such studies in estuaries and bays is much lower. However, in recent years there has been a growing interest in the impact of bridge piers due to anthropogenic development in these areas. Notable exceptions are the study of Miller and Valle-Levinson (1996) on the effects of bridge pilings on stratification and currents in Chesapeake Bay (USA). These authors concluded that there is a significant decrease of stratification locally but not noticeable far from the structure. Moreover, Zarzuelo et al. (2015) analyzed the effect of a bridge on the water exchange of Cádiz Bay, but focusing on channel deepening that was performed simultaneously to its construction. Qiao et al. (2011) evaluated morphodynamic changes, pollutant dispersion, and biodiversity of Hangzhou Bay (China) due to bridge construction.

* Corresponding author.
E-mail addresses: czarzuelo@us.es (C. Zarzuelo), alopez50@us.es (A. López-Ruiz), arnoldo@ufl.edu (A. Valle-Levinson), mdiezm@ugr.es (M. Díez-Minguito), miguelos@ugr.es (M. Ortega-Sánchez).

https://doi.org/10.1016/j.coastaleng.2022.104093
Received 21 December 2021; Accepted 29 January 2022
Available online 12 February 2022

Cádiz Bay (SW Spain) is an estuarine environment in which human interventions have conditioned the estuary's hydro-morphodynamics and environmental status. This bay has had remarkable human interventions in recent decades (Zarzuelo et al., 2015), such as the expansion of the commercial port, the dredging of its navigational channel and the construction of a bridge across the bay which was completed in 2014 (*Constitución de 1812* bridge). This bridge is mainly supported by one pile, which is in the middle of the strait that separates the two main basins of the bay. The tidal and estuarine circulation in this part of the bay is key for its overall health (Zarzuelo et al., 2020) as it controls the water exchange between the basins (Zarzuelo et al., 2015).

This study has the objective of investigating the modifications of *Constitución de 1812* bridge pile on tidal flows at Cádiz Bay strait. Observations and numerical simulations provide information to address this objective. Observations were obtained from two field surveys during semidiurnal tidal cycles along a cross-section that was parallel to the bridge crossing, ~ 200 m landward. Dates of field surveys were selected based on availability of instruments and to minimize the influence of atmospheric forcing.

Measurements during neap and spring tides aimed to explore the effect of fortnightly variations. Numerical results were obtained from a validated and calibrated numerical model (Zarzuelo et al., 2015, 2020, 2021). The effects of the pile on tides are evaluated via the semidiurnal (D2), quarter-diurnal (D4), and sixth-diurnal (D6) tidal bands. The analysis of D2, D4 and D6 bands allows evaluating overtide generation, tidal asymmetries, and their impacts on stratification and sediment transport. Results and discussion presented here can serve as a reference for other bays or estuaries crossed by bridges such as San Francisco Bay (Gross et al., 2009) or Hangzhou Bay (Xie et al., 2013). In addition, results might also help in determining the effects of any other kind of obstacle on tidal wave propagation across estuaries, such as wind farms (Rawson and Rogers, 2015).

The article is organized as follows. The description of the study area is presented in Section 2, followed by the presentation of the data collection and its processing in Section 3. Section 4 describes the results obtained from the harmonic analysis of D2, D4 and D6 bands and tidal asymmetry. The discussion is presented in Section 5, and finally, Section 6 presents the main conclusions.

2. Study area

Cádiz Bay (SW Spain; Fig. 1a) displays 3 regions (Fig. 1b): (A) the outer basin (approx 70 km^2) that opens directly to the ocean, with mean depths of 10 m and gentle bottom slopes, and where two Rivers discharge: San Pedro and Guadalate; (B) Puntales Channel, which is the strait of the bay connecting the outer and inner basins while showing the greatest depths (18 m) and steepest bed slopes; and (C) the inner basin, which is the shallowest zone (approx 50 km^2). Zone C is also connected to the open ocean by a network of creeks (Carraca and Sancti-Petri) of about 18 km in length.

This study examines the effect of the new bridge (*Constitución de 1812* bridge) located at the northern entrance to Puntales Channel (length L = 3.8 km, and width W = 1.3 km; red squares- Fig. 1c), where the bathymetry at its connection with the outer basin is marked by a channel located on the NE margin with the maximum depths. The SW margin exhibits a shallower area of approximately 4 m depth and a shoal of 6–8 m depth at the connection of the channel with the shallower area (Fig. 1d). Puntales Channel is considered dynamically narrow in terms of tides, $W \ll L_t$ being W = 1.3 km the maximum width, and L_t the tidal wavelength, ranges between 280 km and 542 km. The shallow water approximation ($H \ll L_t$) is also satisfied, with H~15 m the mean depth. The barotropic Rossby radius $Ro = \sqrt{gH}/f$ ~ 140 km, verifies $W/Ro \ll A/H$, where A ~ 1.5 m is the tidal amplitude. The bridge has a length of 5 km and a height of 69 m above the mean water level (η), with a maximum span of 512 m. Inside Puntales Channel, seven piers of 20 × 20 m section are located at a depth of 5 m; the largest and easternmost has an area of 60 m × 60 m in a depth of 15 m. This pier was previously studied as possibly affecting the estuarine dynamics of Cádiz Bay (Zarzuelo et al., 2015). The other smaller piles, also being over the shallower zone, do not interfere with the dynamics as it was shown in previous studies (Zarzuelo et al., 2015, 2017).

Tidal forcing in the bay is predominantly semidiurnal, being the M2 the constituent with the largest amplitude (Zarzuelo et al., 2015). The superposition of M2 and the other semidiurnal constituents S2 and N2, altogether forming the D2 band, generates fortnightly and monthly variations in the currents. Ocean tides generate higher-frequency overtides when propagating in shallow areas, and nonlinear terms associated with friction and continuity are responsible for the quarter-diurnal (D4) and sixth-diurnal (D6) bands, among others (Parker, 1991; Aubrey and Speer, 1985). Two primary waves propagating through a nonlinear medium generate new harmonics with frequencies that are sums or differences of the primary frequencies. The D2 constituents give rise to higher levels of harmonics generation (e.g., the overtide, D4 and D6). The superposition of D2 and D4 creates tidal ebb–flood asymmetry in levels and currents (Aubrey and Speer, 1985; Valle-Levinson et al., 2004) and affects the transport of sediment, water and other pollutants. The influence of the D4 bands plays an essential role in the bay, especially in the Puntales Channel, due to bottom friction and geometry complexity at the strait. As the tide propagates into Cádiz Bay, friction increases and subsequently distorts the tidal wave as it moves landward, thereby producing a tidal asymmetry. The tidal wave is nearly symmetric at the entrance of the bay (basin A of Fig. 1b). In addition, the convergent widths of Cádiz Bay between basins B and C (Fig. 1b) causes the tidal wave to amplify slightly along the Puntales Channel (Zarzuelo et al., 2015, 2017). However, as the tidal wave propagates through the bay, it becomes flood dominant (Zarzuelo et al., 2015).

Regarding its water column structure, the bay is partially-mixed, circulation is controlled by atmospheric, tidal, and buoyancy forcing, as well as by its complex morphology and bathymetry (Zarzuelo et al., 2020). Wind works on the estuary at a scale R of 0.03 days:

$$R_{\text{wind}} = \frac{\mu}{t_{\text{wind}}} \frac{V_{\text{wind}}}{\text{Vol}} \tag{1}$$

baroclinicity from buoyancy produces a scale of 24.4 days:

$$R_{\text{bar}} = A\sqrt{\frac{(\Delta\rho/\rho)\, g h}{4\text{Vol}}} \tag{2}$$

and tidal forcing exchanges water at 1.2 days:

$$R_{\text{tide}} = \frac{\mu}{t_{\text{tide}}} \frac{\text{Vol}_{\text{prism}}}{\text{Vol}} \tag{3}$$

In Eqs. (1)–(3), μ is the retention coefficient ($\mu = \left(\delta S_{tide}/\Delta S\right)\left(Vol/Vol_{prism}\right)$, being δS_{tide} the variation of salinity for a tidal cycle), t_{wind} and t_{tide} are the characteristic periods of wind and tide, ρ is the water's density, h is the mean depth, g is the gravity acceleration, $\text{Vol}_{\text{prism}}$ is the tidal prism, V_{wind} is the water volume variation due to wind and Vol is water volume of the outer bay. Wind influence on the bay is seasonal, with predominantly NW-NE winds in winter and SW-W winds during summer. The most energetic wind events are the NW, which, together with the flood and ebb period in spring tides, cause the maximum mobilization of water (Zarzuelo et al., 2017).

Cádiz Bay densimetric tidal Froude number ($Fr^2 = U_0^2/(g'h)$, Valle-Levinson, 2021) is ~ 1, and its Ekman number ($Ek = Az/(fh^2)$, Valle-Levinson, 2021) is also ~ 1. Cádiz Bay is density-driven and vertically sheared during neap tides ($Ek > 1$, $FR^2 < 1$, Valle-Levinson, 2021), where g' is the reduced gravity, U_0 is the velocity amplitude, Az is the kinematic eddy viscosity, and f is the Coriolis parameter. Thereby, Cádiz Bay is tidally driven and laterally sheared during spring tides.

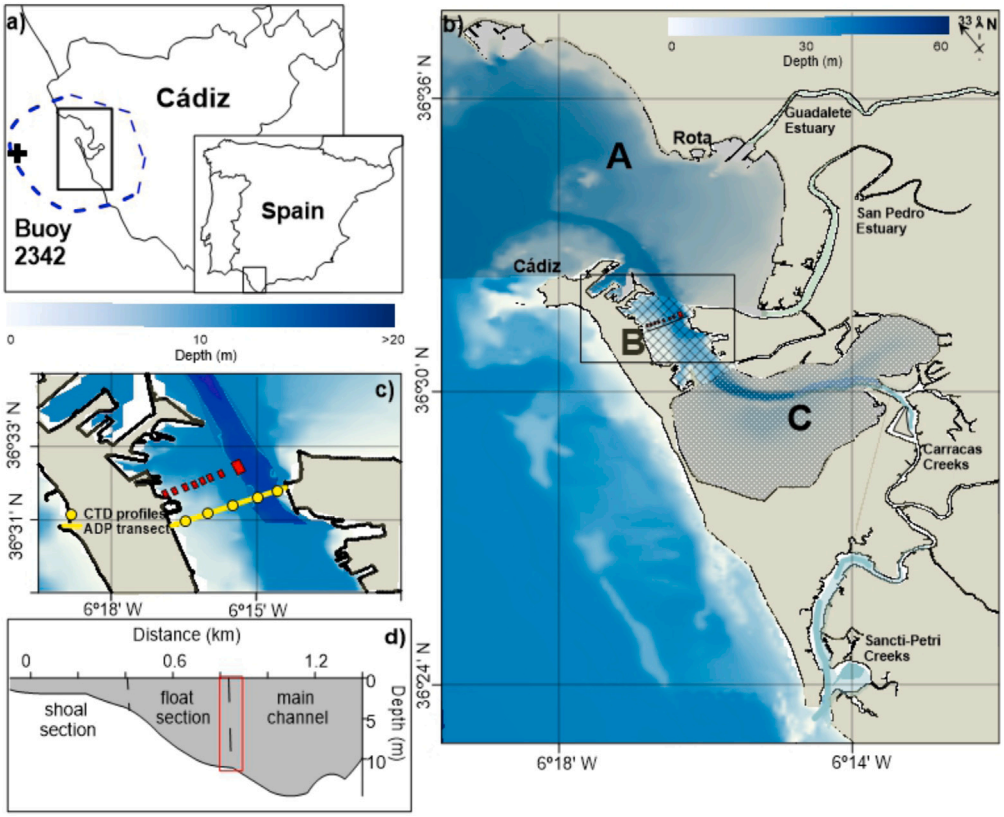

Fig. 1. Study area in Cadiz Bay. Panel (a) Location of the study area (bold black box), and the limits of the computational model grid (blue dashed line), Panel (b) Study area and zonation of the three basins of influence, Panel (c) detail of Puntales Channel where the field survey were carried out. The cross-section is identified by the yellow line. Yellow circles indicate the location of the CTD profiles. Red rectangles in (c) denote the piers (small rectangles) and pile (largest rectangle) of *Constitución de 1812* bridge and (d) bathymetric profile of the cross-section, marking in red the bridge pile.

3. Methods

3.1. Data collection and processing

A vessel-towed (RD Instruments 1200 kHz) and an ADP (Sontek 1000 kHz) were used to sample during two 13-h field surveys. Surveys were conducted during neap tides (3 July 2013) and spring tides (22 August 2013) at the entrance of the Puntales Channel. Measurements were collected along a 1.3-km cross-bay transect landward of the bridge (yellow line- Fig. 1c). Velocity profiles were collected every 5 s, with a vertical resolution (bin size) of 0.5 m. Navigation was carried out with a Global Position System (GPS), which was used to correct the bottom track velocities. The cross-bay transect was the same in the two surveys. Data from the RDI instruments are not shown in the manuscript, although they were used to double check ADP measurements.

A total of 24 and 27 paths along the section were sampled for the neap and spring 2013 surveys, respectively. In addition, during the two field surveys conducted during 2013, profiles of temperature and salinity were taken simultaneously with the velocity measurements along the entire section, 300 m apart from each other (yellow dots- Fig. 1c). These profiles were measured with a CTD (SBE-BIRD 19 Plus), with four samples per second. The CTD profiles were obtained 5 times at each station during each tidal cycle.

For processing data, the vessel velocity recorded by the GPS was used to correct the bottom track velocity. In addition, 10% of the near-bottom measurements were eliminated because of side lobe effects, as well as data with a signal return of less than 85%. Velocities with vertical velocity errors above 5% of the maximum flow (approximately 2% of the raw data) were excluded. Finally, 10% of the surface values were removed to omit error due to tidal range. The obtained current values were interpolated to a uniform grid along the section, length 1.3 km and maximum depth 16 m, with a periodicity of 20 min. The spacing between horizontal and vertical cells was 15 m (90 points) and 0.5 m (28 points), respectively.

Table 1
Summary of characteristic climate values collected during the field surveys.

	Tidal range [m]	Wind velocity [m/s]	Wind direction [°]	Atmospheric Pressure [HPa]
Neap tide (2013 Jul 03)	1.60	3 ± 1	NW-NE	1016 ± 2
Spring tide (2013 Aug 22)	3.60	4 ± 2	NW-NE	1017 ± 3

Tidal and atmospheric conditions (wind speed, wind direction, and atmospheric pressure) during each field survey are listed in Table 1. During neap tides, the tidal range was 1.6 m, with average wind speeds between 2 and 4 m/s, mainly northwesterly to northeasterly, and atmospheric pressure values around 1016 hPa. Spring tides show very similar wind and atmospheric pressure conditions, but tidal range was 3.6 m.

3.2. Numerical modeling

The numerical model used in this study is DELFT3D-Flow (Lesser et al., 2004), a three-dimensional finite-difference hydrodynamic model developed for coastal and estuarine systems by the University of Delft. It solves the 3D baroclinic Reynolds-Averaged Navier–Stokes and transport equations under shallow-water and Boussinesq assumptions. Previous studies in Cádiz Bay used the numerical model to analyze the impact of other human interventions on hydrodynamics (Zarzuelo et al.,

2015), on morphodynamics (Zarzuelo et al., 2017), and to analyze the dynamics of the bay (Zarzuelo et al., 2020, 2021).

The grid used is the same (Fig. 1a) as in previous studies, being curvilinear grid with an average cell value of 200 × 200 m and 60 × 60 m on average in the Puntales Channel (Zarzuelo et al., 2020, 2021). This discretization allows defining the pier section as a drypoint, where the velocity at the centroid of the cell is set to zero and no flux is allowed through the cell side boundaries. The vertical grid discretization is defined as 10 σ-layers (their thickness are 2, 10, 10, 10, 18, 18, 10, 10, 10, 2% of the water depth).

The model has been forced with 18 main harmonic constituents obtained from the Oregon State Tidal Prediction model (Egbert and Erofeeva, 2002). Wind data have been included from Buoy 2342 (Fig. 1a) of Puertos del Estado. River discharge has been specified according to the mean values of river discharge of the San Pedro and Guadalete rivers. Implemented with the model's heat module, simulations of water temperature and salinity fields have been described in Zarzuelo et al. (2021).

In Zarzuelo et al. (2019) the 3D model was calibrated for tidal velocities obtaining R^2 coefficients of 0.67 and 0.88 for the field survey 2015. Zarzuelo et al. (2021) calibrated the heat transfer modules, which are necessary to know the density variation along the water column. A value as high as $R^2 \sim 0.67$ was obtained. The same setup used in those studies has been used to test them. Four months (June–September 2013) have been simulated to cover the two field surveys carried out during 2013. The month of June serves as spin-up. In particular, the data used to validate the model are those from spring 2013, with correlation coefficients $R^2 \sim 0.71$ for the velocity M2 amplitude.

3.3. Data analysis

Observations were analyzed to focus on (1) the transverse variability of the tidal flow produced by the interaction of tidal currents in the bay strait; and (2) the effects produced by the main pile of the bridge. Numerical model results are used to check if the tidal flow behavior is due to the bridge-piling effect or not, by forcing the model without and with the pier section. A tidal harmonic analysis was performed using the T_TIDE tool (Pawlowicz et al., 2002) to obtain the tidal ellipses of the semi-diurnal (D2, angular frequency (w) of $1.41 \cdot 10^{-4}$ rad/s), quarter-diurnal (D4, $w = 2.80 \cdot 10^{-4}$ rad/s), and sixth-diurnal (D6, $w = 4.21 \cdot 10^{-4}$ rad/s) bands. The behavior of each tidal ellipse parameter (semi-major axis, semi-minor axis, inclination, and phase) was analyzed to characterize tidal patterns in the cross-section, thus highlighting the possible differences between neap and spring tides. Tidal asymmetry changes were investigated along the cross-section, depending on the depth and location of the pile of the bridge. In addition, the relative tidal phases $2\phi_{D2} - \phi_{D4}$ and $3\phi_{D2} - \phi_{D6}$ were also used to describe the tidal distortion, determining when the flood dominates (90–270°) or ebb dominates (0–90° or 270°-360°) the flow (Blanton et al., 2002). These tidal asymmetry conditions are strongly related to the morphology of tidally dominated bays. When flood dominates, sediment is transported landward, whereas the opposite occurs when ebb dominates.

4. Results

Before analyzing the results, the main hydrodynamic characteristics given during the dead (black line- Fig. 2) and live (red line- Fig. 2) field campaigns will be discussed. In the neap field survey a tidal range of 1.5 m is observed (Fig. 2a), with maximum east velocities of 0.5 m/s (Fig. 2b) and 0.2 m/s in the north direction (Fig. 2c), while in the spring field survey its tidal range reaches 3.2 m (Fig. 2a), with east and north velocity 1.5 m/s and 0.4 m/s, respectively (Figs. 2b and c). The density conditions (Fig. 2d) vary 0.8 kg/m^3, being lower in the neap field survey.

Table 2
Mean results of the tidal ellipses parameters of the D2, D4 and D6 bands in the cross-section. The relative differences between with and without piles of semi-major and semi-minor axis are calculated as *(spring-neap)/neap*. The absolute differences of inclination and phase are calculated as *(spring-neap)*.

		Shallow	Pile wake	Pile	Main Channel
M_{D2} [m/s]	Spring tide	0.25	0.35	0.40	0.42
	Neap tide	0.10	0.12	0.13	0.16
	Variation	150%	191%	185%	180%
$\|m_{D2}\|$ [m/s]	Spring tide	0.08	0.08	0.02	0.10
	Neap tide	0.07	0.07	0.01	0.07
	Variation	14%	14%	100%	43%
I_{D2} [°]	Spring tide	70	120	100	110
	Neap tide	70	120	100	110
	Variation	0°	0°	0°	0°
ϕ_{D2} [°]	Spring tide	180	70	50	70
	Neap tide	280	230	210	220
	Variation	−100°	−60°	−60°	−50°
M_{D4} [m/s]	Spring tide	0.10	0.12	0.16	0.14
	Neap tide	0.06	0.06	0.12	0.10
	Variation	67%	100%	33%	40%
$\|m_{D4}\|$ [m/s]	Spring tide	0.03	0.05	0.02	0.07
	Neap tide	0.02	0.03	0.01	0.05
	Variation	50%	67%	100%	40%
I_{D4} [°]	Spring tide	50	140	130	150
	Neap tide	150	100	110	100
	Variation	−100°	40°	20°	50°
ϕ_{D4} [°]	Spring tide	300	100	220	210
	Neap tide	100	80	100	100
	Variation	200°	20°	120°	110°
M_{D6} [m/s]	Spring tide	0.10	0.08	0.10	0.12
	Neap tide	0.08	0.05	0.08	0.08
	Variation	25%	175%	33%	50%
$\|m_{D6}\|$ [m/s]	Spring tide	0.04	0.02	0.04	0.04
	Neap tide	0.01	0.02	0.03	0.03
	Variation	300%	0%	33%	33%
I_{D6} [°]	Spring tide	100	80	80	120
	Neap tide	20	100	40	40
	Variation	80°	−20°	40°	80°
ϕ_{D6} [°]	Spring tide	220	230	250	240
	Neap tide	170	180	220	220
	Variation	50°	50°	30°	20°

The observed results are presented here, being the bay tidally driven and laterally sheared in spring tides whereas density-driven and vertically sheared in neap tides. The numerical results have only been used to check whether the tidal flow behavior is produced by the pile location or by other, which is discussed in Section 5.

4.1. Harmonic analysis

The characteristics of the D2, D4 and D6 tidal ellipses during spring and neap tides are shown in Table 2, extracted from Figs. 3–5.

Fig. 3a.1 shows that for neap tide the maximum D2 semi-major axis is reached in the cross-section of the main channel (0.16 m/s), decreasing around the pile. The lowest values are observed in shallow areas and in the wake of the pile (Table 2). The values decrease with depth, especially in the cross-section of the main channel, where the most significant decrease is observed (from 0.15 m/s to 0.06 m/s). The semi-major axis spatial variability in the cross-section is the same at neap as spring tide, only the magnitude is amplified by 180% (Fig. 3a.2). This increase is due to the difference in tidal range between spring tide (3.6 m) and neap tide (1.6 m) (Table 1). Note that in the pile area, its value decreases strongly for neap and spring tides (Table 2).

The observed D2 semi-major axis values are more than twice those of the D2 semi-minor axis (Fig. 3b), so eccentricity amplitude is relatively low degenerating almost into a straight line. The maximum absolute values of the semi-minor axis for neap tide (Fig. 3b.1) are

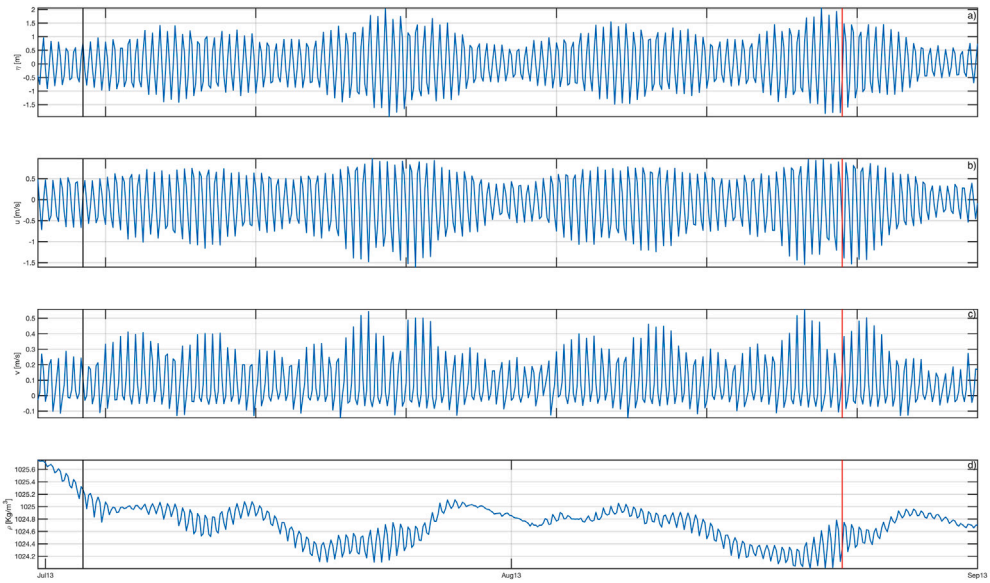

Fig. 2. Hydrodynamics characteristic during the field surveys. Panel (a) water level, panel (b) east velocity, panel (c) north velocity and panel (d) density. Black and red lines correspond to neap and spring field survey, respectively.

reached in the part of the cross-section of the pile wake and the main channel (0.07 m/s). Negative sign indicates that ellipses rotate clockwise. A clockwise rotation is observed at the surface up to 6 m depth in the cross-section of the main channel and 4 m in the pile wake. In the rest of the cross-section, counterclockwise rotation predominates. The transition between 3 and 5 m, where the rotation of the ellipses changes direction, suggests the possible location of the pycnocline or the influence of topography. Again, the same semi-minor axis behavior occurs during spring tides as during neap tides (Fig. 3b.2), the only difference is found in the part of the cross-section of the main channel (Table 2).

Results also indicate predominant along-channel D2 orientations of ~110° from the East (Fig. 3c). Deviations from the channel alignment are found in the bottom and over the portion of the cross-section affected by the wake of the pile (120°). For the D2 phases at neap tide (Fig. 3d.1), the highest values are reached in the shallower areas (280°), with a difference of 60° with respect to the cross-section of the main channel, corresponding to a phase lag of almost 2 h between these two parts of the cross-section. In the part of the cross-section affected by the pile, there is a decrease of 20° with respect to the cross-section of the main channel (40 min), while in the deeper parts there is a slight increase of 10° (20 min). At spring tide (Fig. 3d.2; Table 2), phases affected by the pile result in differences of 3.4 h between the pile portion and other parts of the section.

For the D4 and D6 bands, for both spring and neap tide, the semi-major axis is smaller for D4 (Fig. 4a) and D6 (Fig. 5a) than for D2 (Fig. 3a), the difference being more noticeable in spring tide (second column in Figs. 4 and 5). The reduction is not that high during neap tide (first column in Figs. 4 and 5). This is due to the greater influence of the frictional terms in tidal propagation ($|(U_0|U_0|)/(H+\eta)|_{neap} < |(U_0|U_0|)/(H+\eta)|_{spring}$; 0.002 < 0.009).

The D4 semi-major axis highest values are in the cross-section of the main channel and around the pile (Table 2). The semi-major axis of the D6 band shows the highest values in the pile (neap tide: 0.08 m/s, spring tide: 0.1 m/s) with a reduction in the wake (neap tide: 0.05 m/s, spring tide: 0.08 m/s). The D4 semi-minor axis (Fig. 4b) is weakly reduced (10%) compared to D2, while the D6 semi-minor axis (Fig. 5b) decreases up to 0.02 m/s (70%). The rotation of the ellipse is maintained in the case of spring tide, although for neap tide there is a change of direction, which is especially relevant around the pile and in the shallower zones. The inclination of the ellipses (Figs. 4c and 5c) is parallel to the alignment of the channel, with rotations on the surface and close to the pile (reduction of 40°-80°). The phases of the D4 and D6 bands (Figs. 4d and 5d, respectively) reach their maximum in the wake of the pile and the shallower areas. Also note how the phases for D4 and D6 are larger during spring than during neap tide (Table 2).

Table 3
Mean results of the tidal asymmetry in the cross-section. The differences of the ratios are calculated as (spring-neap)/neap. The differences of phases are calculated as (spring-neap).

		Shallow	Pile wake	Pile	Main Channel
D4/D2	Spring tide	0.20	1.10	0.30	1.60
	Neap tide	0.50	0.70	0.50	1.30
	Variation [%]	−80	57	−40	23
D6/D2	Spring tide	0.40	1.70	1.10	0.50
	Neap tide	0.50	0.60	1.50	1.00
	Variation [%]	−20	183	−27	−50
$2\phi_{D2}-\phi_{D4}$	Spring tide [°]	200	270	290	280
	Neap tide [°]	200	250	290	240
	Variation [°]	0	20	0	40
$3\phi_{D2}-\phi_{D6}$	Spring tide [°]	200	220	220	210
	Neap tide [°]	200	220	220	230
	Variation [°]	0	0	0	−20

To determine whether the three bands (D2, D4 and D6) are sufficient to assess the section's hydrodynamic behavior, the velocity field was reconstructed using only these bands. The reconstructions have been compared to observations at each grid point of the cross section, and have been assessed with their determination coefficient R^2. Calculations showed that the tidal signal is reproduced almost entirely (92%) considering only these three bands (Fig. 6). Minor differences are only relevant in the shallow zone and the deeper cells, possibly due to signal noise or other forcings (such as wind) that can produce incomplete reproduction.

4.2. Tidal asymmetry

Tidal asymmetry indicators are presented in Table 3 for spring and neap tides, extracted from Figs. 6 and 7.

Asymmetry values show that maximum D4/D2 ratios (1.3, Fig. 7a) were observed in the main channel, while maximum D6/D2 (0.7, Table 3) were found in the pile wake (Fig. 7c). Increased D6/D2 in

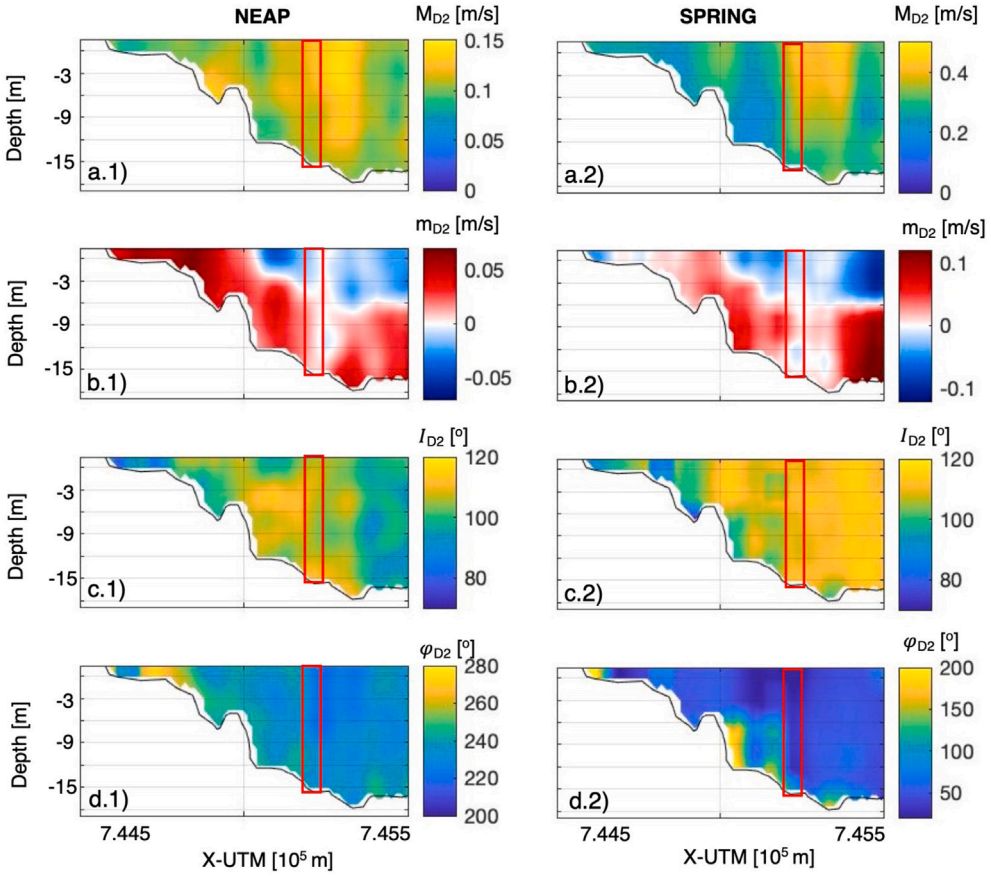

Fig. 3. Semi diurnal (a) Semi-major axis M, (b) Semi-minor axis m, (c) inclination I and (d) phase ϕ of the tidal ellipse for neap tide (first column) and spring tide (second column). The red square indicates the part of the cross-section closest to the bridge pile.

spring tides relative to neap tides indicated greater asymmetries as the tidal elevation increases. At spring tide (Fig. 7b and 7c, for D4 and D6 respectively) the maximum asymmetry values were mostly found around the pile wake, being higher for D6 than for D4 (1.7 and 1.1, respectively). Comparing spring and neap tides (Table 3), the largest changes were observed in the pile wake, where the D6 band increased 183% (Fig. 7c and 7d).

Phase asymmetry calculated with the D4 and D6 bands at neap tide showed flood-dominance (Figs. 8a and 8c) with a slight variation toward ebb-dominance in the wake of the pile and at the bottom. In spring tide (Fig. 8b and 8d), the highest values were also found in the wake of the pile, corresponding to ebb dominance. In the rest of the cross-channel section there was flood dominance. Results showed changes in the cross-section for the D4 band, where it displayed flood and ebb dominance in the channel but vanishing small changes in the pile wake.

5. Discussion on bridge-piling effects

Results are discussed in terms of the influence of the pile on (1) tidal harmonics, (2) stratification and (3) sediment transport. To discuss the effect of the pile, the numerical model was used to compare simulations with and without the pile. The most important differences on tidal flow between neap and spring tides with and without pile at estuary strait are summarized in Table 4.

5.1. Tides

The bridge pile reduced the D2 current amplitude and modified the phase as shown in Fig. 3. Fig. 9a.1 and b.1 compare observations and model results for the amplitude D2 at spring tide, under present

Table 4
Summary of the main results the cross-section considering the influence of the bridge pile.

		Pile	No Pile	Variation
TidalHarmonics	u_{D2} [m/s]	0.30	0.45	−50%
	ϕ_{D2} [°]	120	90	30°
	u_{D6} [m/s]	0.08	6	100%
Stratification	Location of the pycnocline [m]	4–6	9	1 m
Sediment Transport	Q_y [m^3/s^2]	0.1	12	−63/%

conditions. In contrast, Fig. 9c.1 illustrates the results for a numerical simulation without the pile. For the no-pile scenario, the D2 current amplitude at the location of the pile is 50% higher. Therefore, the pile reduces tidal flow (Table 4) and, overall, alters the flows in the cross-section. The Fig. 9b.2 shows that D2 phases are generally well reproduced by the model (Fig. 9-second column). Over the shoal, however, there is a variation of 30° that is attributed to morphological complexities and possible model inaccuracies in this area and to the small R^2 compared to the rest of the cross-section (Fig. 6). Notably, the D2 phases exhibit a lag between the tidal currents in the cross-section of the main channel and those of the shoal, as observed in Fig. 3d.2. When compared with the modeled data without the pile (Fig. 9c.2), the lag produced by the pile disappears, and the phase value remains practically constant throughout that portion of the cross-section. This shows clearly that the pile distorted the tidal flows.

The bridge pile also caused an increase of overtidal amplitude (as shown in Figs. 4 and 5). Maximum D4 and D6 amplitudes appeared at the pile wake because of increased of lateral gradients (lateral shears)

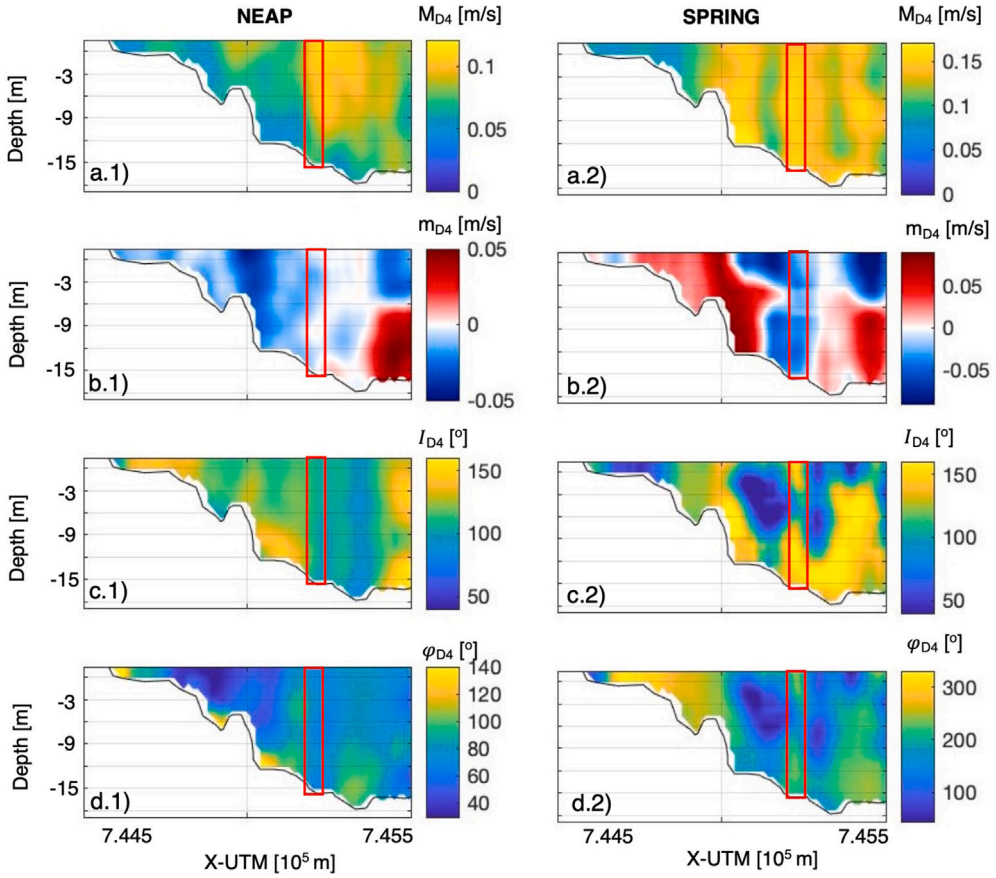

Fig. 4. Quarti-diurnal (a) Semi-major axis M, (b) Semi-minor axis m, (c) inclination I and (d) phase ϕ of the tidal ellipse for neap tide (first column) and spring tide (second column). The red square indicates the part of the cross-section closest to the bridge pile.

in the tidal currents (Figs. 4a and 5b, respectively), i.e., advective accelerations generating overtides (e.g. Parker (1991)). Their amplitudes were also prominent over shoals because of the increase of effective bottom friction (Parker, 1991). The D4 and D6 phases changed with increasing depth and varied sharply in the wake of the pile (Figs. 4d and 5d, respectively). Tidal asymmetries were higher around the pile wake and at the bottom, being more relevant for the D6 band (Figs. 7a and 7d). This result indicates that D6 amplitude is larger than that of D4, unlike other study areas, such as Damariscotta River (Lieberthal et al., 2019), where the opposite occurs. The fact that D6 amplitude is larger than that of D4 response highlights the importance of bottom friction in the momentum balance. Similar results were found in the Gironde Estuary (Ross and Sottolichio, 2016), where the influence of D6 amplitude was found in zones with abrupt depth changes. Finally, flood dominance is observed except in the wake of the pile and near the bottom (Fig. 8). The largest changes are found during spring tides, the bridge pile (more asymmetry) and around the wake of the pile, changing from flood to ebb dominance.

The D6 amplitude in the whole cross-section was also calculated with the numerical model, both with and without the pile (Fig. 10), to determine the pile influence. The same was done for D4 (not shown). Firstly, comparison between observations and modeled results for spring 2013 yields an $R^2 \sim 0.67$, showing reliable representation derived from observations (the shallow zone is excluded). The D6 amplitude increase over the pile wake is still noticeable, as well as a D6 amplitude reduction in the main channel. The D6 amplitude increase is not observed in the numerical results without the bridge pile, being the values practically constant (0.03–0.04 m/s) over almost the entire section (Fig. 10). Therefore, it can be concluded that the presence of the pile yields the increase of D6 amplitude, which results in a distortion of the tidal wave due to the presence of the pile.

5.2. Stratification

The location of the pycnocline of the main channel at the strait is inferred at depths between 3 and 5 m, from the analysis of the D2 semi-minor axis (Fig. 3b). According to Souza and Simpson (1996), the boundary layer thickness can be estimated for a clockwise ($\delta_- = \sqrt{2N_z/(w-f)}$) and counterclockwise ($\delta_+ = \sqrt{2N_z/(w+f)}$) rotation, where ω_{D2} is the characteristic angular frequency of the D2 band, f the Coriolis parameter ($8.6791 \cdot 10^{-4}$ rad/s) and N_z the eddy viscosity parameter (0.005 m^2/s). The values obtained are $\delta_- \sim 4$ m and $\delta_+ \sim 1$ m. The results show that the thickness of the frictional layer for the counterclockwise rotation is similar to the location of the pycnocline calculated with the ellipticity (3–5 m, Fig. 4b). In terms of the tidal ellipses, the surface current ellipses thus acquire a clockwise rotation, while the near bottom current ellipse becomes more anticlockwise (Fig. 3) due to a reduction in the clockwise component associated with frictional influence below the pycnocline. The value of the Richardson number, $Ri=(g \cdot h \cdot \Delta\rho)/(\rho \cdot U^2)$, also shows the importance of ellipticity since its value is 0.67 and therefore with a partially stratified estuary. For comparison, Simpson et al. (1993), Simpson and Souza (1995), Souza and Simpson (1996) showed that Richardson values greater than 1 correspond to periods of higher stratification and lower mixing, resulting in a deeper pycnocline.

Estimates of the pycnocline position from the ellipticity (blue line- Fig. 11) are corroborated by the echo anomaly (orange line- Fig. 11). The echo anomaly ($EA = 10\log(\text{Echo}) - < 10\log(\text{Echo}) >$) is calculated to determine the possible position of the pycnocline, which is obtained through the echo measured with ADCP (Valle-Levinson et al., 2004; Ross et al., 2014). The vertical gradient of the normalized echo anomaly or EA highlights the possible presence of the pycnocline. According to our results, sporadic patches of high values of the vertical gradient (1

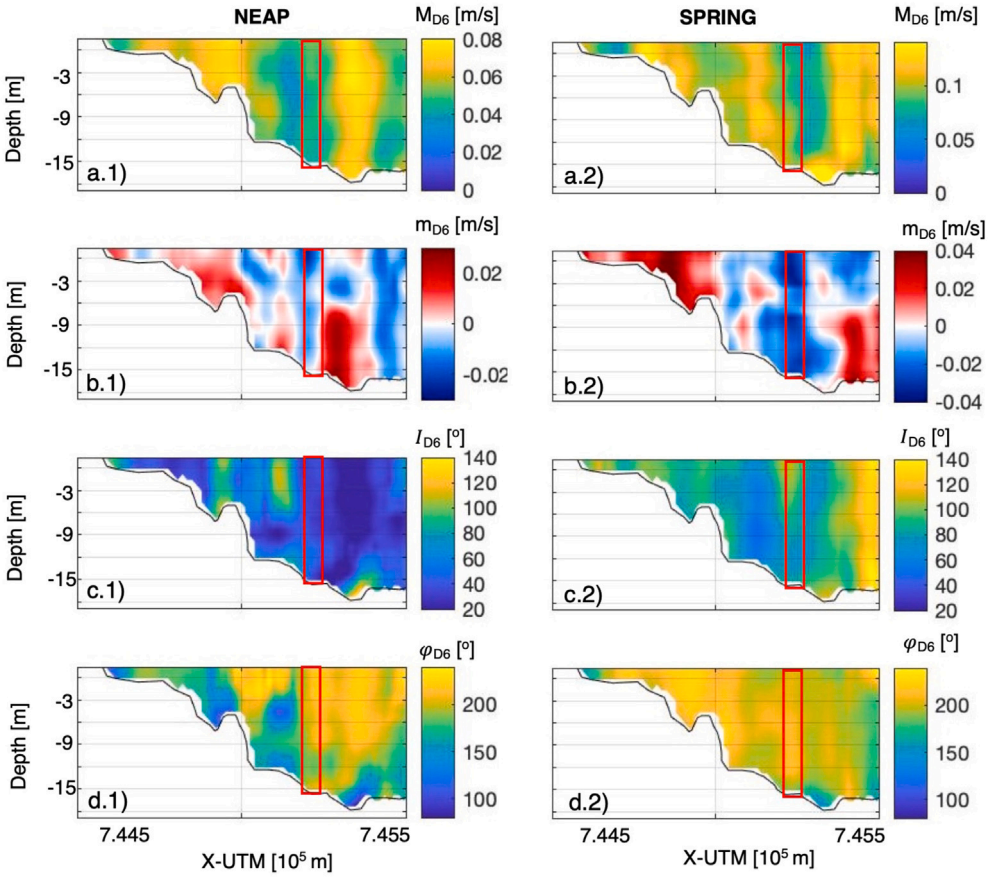

Fig. 5. Sixth-diurnal (a) Semi-major axis M, (b) Semi-minor axis m, (c) inclination I and (d) phase ϕ of the tidal ellipse for neap tide (first column) and spring tide (second column). The red square indicates the part of the cross-section closest to the bridge pile.

db/m) were identified around the inferred location of the pycnocline in both field surveys conducted (Fig. 11). The numerical model results of the ellipticity without considering the bridge pile (yellow line- Fig. 11) show that the location of the pycnocline is very similar to that analyzed previously, except at the bridge pile, where it undergoes a decrease of the pycnocline of approximately one meter.

The data presented in Sections 5.1 and 5.2 based on field data suggest a flow distribution as sketched in Fig. 12, where the diagrams synthesize tidal and stratification features for neap and spring tides. The pycnocline, located between 4–6 m depth, delimits the change of ellipticity sign that rotate clockwise in the upper layer and counterclockwise in the lower layer. The main difference between neap and spring tides is the change of dominance between flood and ebb. At neap tide, flood dominance is observed in the entire main channel, except in the area of the bridge wake. At spring tide, the flood tide is dominant in the upper 5 m of the cross section, while there is ebb dominance at near the bottom, at the wake of the pile, and in the shallowest areas of the cross-section.

5.3. Potential sediment transport

There is a close relationship between tidally induced sediment transport and tidal asymmetry. Therefore, the pile is expected to influence the residual sediment transport. Bagnold (1963) developed a theory based on energetic balance that relates residual sediment transport rate, Q, to the work done by the fluid current $\vec{u} = (u, v)$ at the bottom (being along and across channel velocity, respectively). Other formulations generalized this approach considering the net transport to be proportional to a certain power of the flow, typically between 3 and 6, or for depth-integrated horizontal sediment transport (e.g. Dronkers, 1986; Hoitink et al., 2003). Only the vertical averaged is analyzed here, in order to determine sediment transport paths, which allows to determine the gain or loss of sediment due to the location of the pile.

According to Hoitink et al. (2003), the residual transport due to a steady current, defined as the time-average of Q, $\overline{Q}$, reads

$$\overline{Q} \propto U_\infty^3 \equiv \lim_{t\to\infty} \frac{1}{T} \int_0^T u|u|^2 dt \tag{4}$$

Vertically averaged residual sediment transport along the main channel (Q_x, positive seaward and negative ladward) induced by a tidal wave comprised only of D2, D4 and D6 harmonic bands is evaluated with Eq. (4) at neap and spring tide (Fig. 13). The highest transport values are found at the main channel, being less relevant in the area of the pile and its surroundings. Values increase during spring tides (orange line- Fig. 13) with respect to neap tides (blue line- Fig. 13). The portions with largest values correspond to areas with the largest tidal asymmetries (Fig. 7). It can be concluded that in these areas there is a greater potential sediment transport. The residual sediment transport is also inspected without considering the bridge pile in the numerical model (yellow line- Fig. 13). All values are practically the same than the observed data. Near the location of the pile (red line- Fig. 13), the residual sediment transport decreases by almost 63% (Table 4). Therefore, it can be concluded that the pile works as an obstacle to sediment flow. In the part of the main channel of the cross-section, the transport is landward. Seaward net residual transport appears in the wake of the pile and in the part of the shallower zone.

6. Conclusions

This work investigates the effects of the presence of a bridge pile on the tidal flow at the strait of the Cádiz Bay (Spain). Observations results

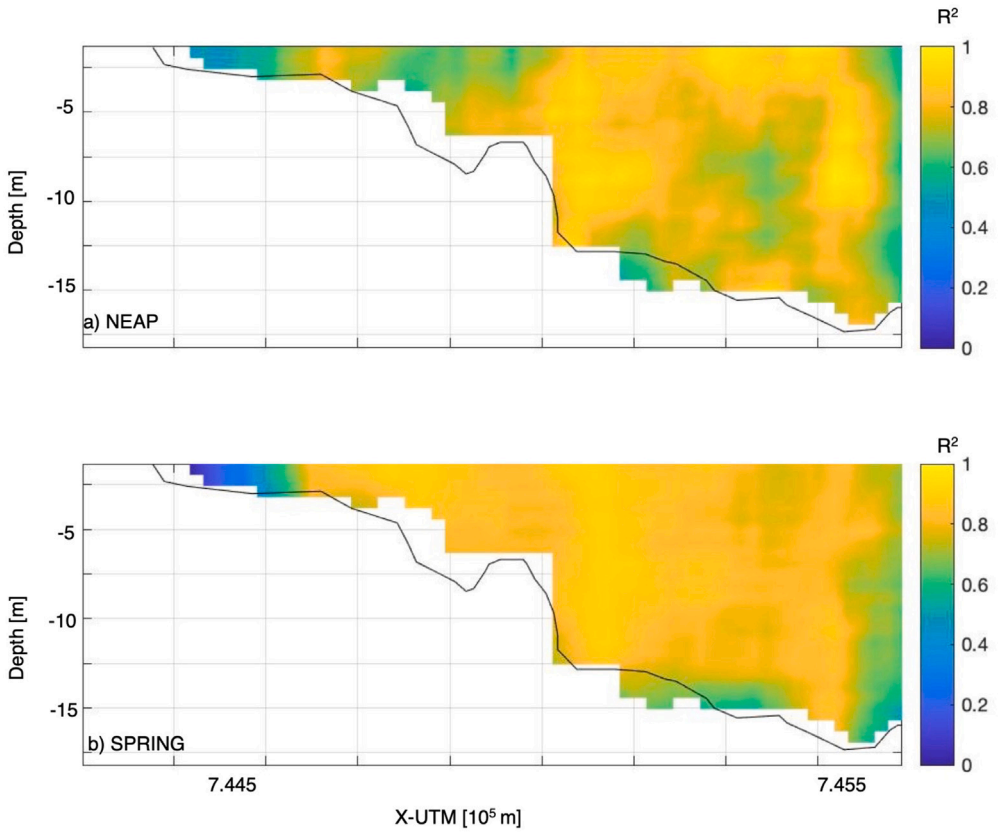

Fig. 6. Determination coefficient R^2, or variance explained by fit, between measured and reconstructed signal with bands D2, D4, and D6 for neap tide (a) and spring tide. Values of 1 correspond to a perfect fit.

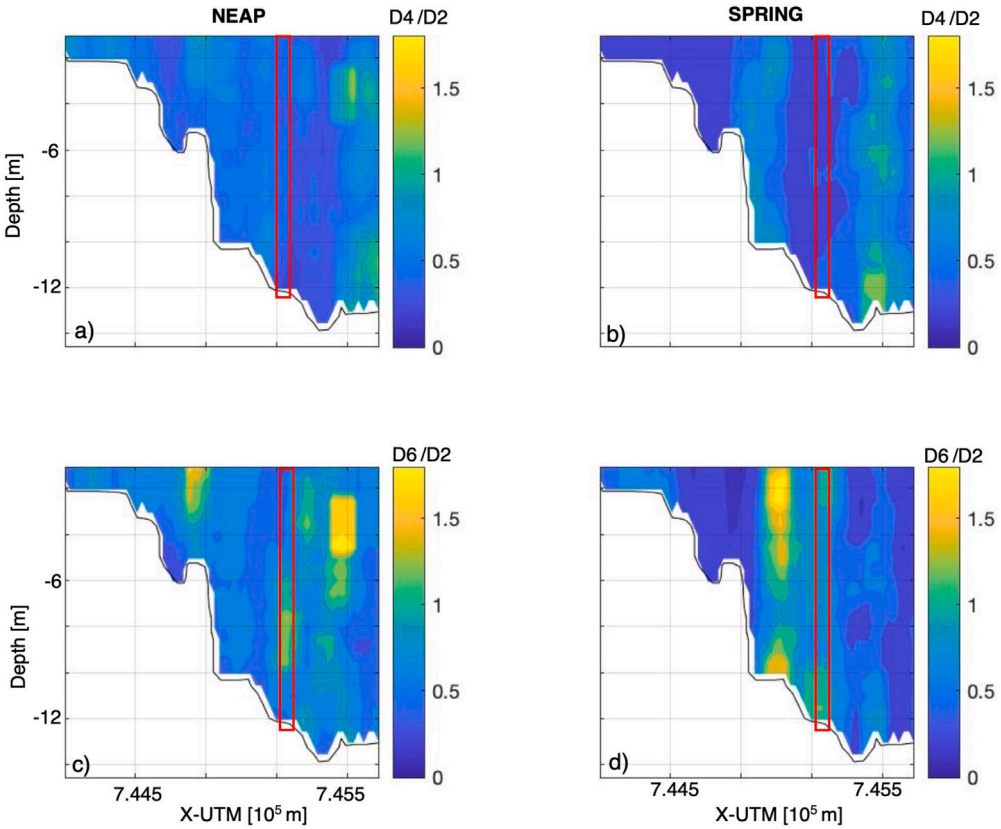

Fig. 7. Tidal asymmetry for the neap tide, (a) D4/D2 and (c) D6/D2. Tidal asymmetry for the spring tide, (b) D4/D2 and (d) D6/D2. The red square represents the pile.

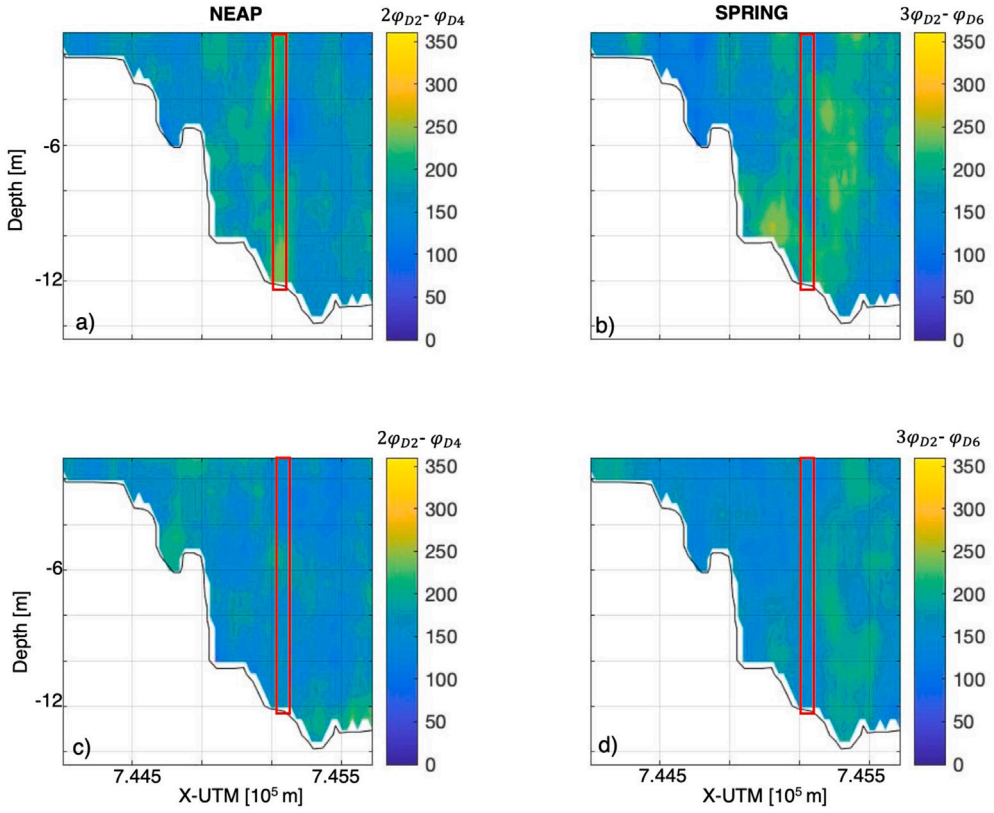

Fig. 8. Flood (90°-270°)-ebb (<90°>270°) dominance for the neap tide, (a) $2\phi_{D2}$ - ϕ_{D4} and (c) $3\phi_{D2}$ - ϕ_{D6}. Flood (90°-270°)-ebb (<90°>270°) dominance for the spring tide, (b) $2\phi_{D2}$ - ϕ_{D4} and (d) $3\phi_{D2}$ - ϕ_{D6}. The red square represents the pile.

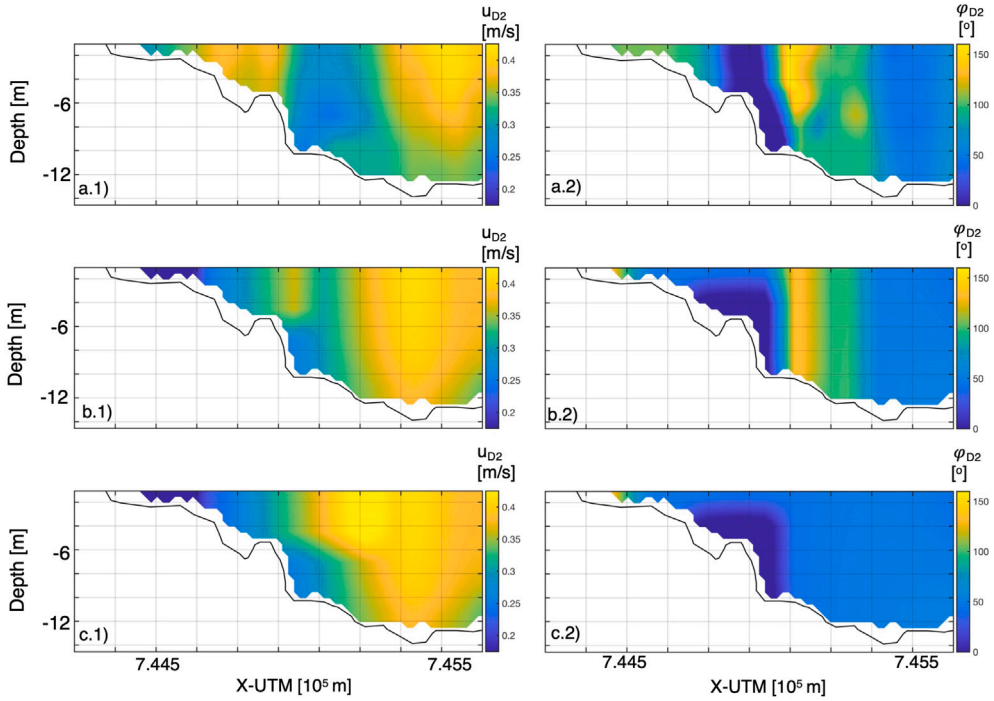

Fig. 9. Amplitude (first column) and phase (second column) of D2 during the spring tide (a) observed (b) modeled with the bridge pile and (c) modeled without the bridge pile.

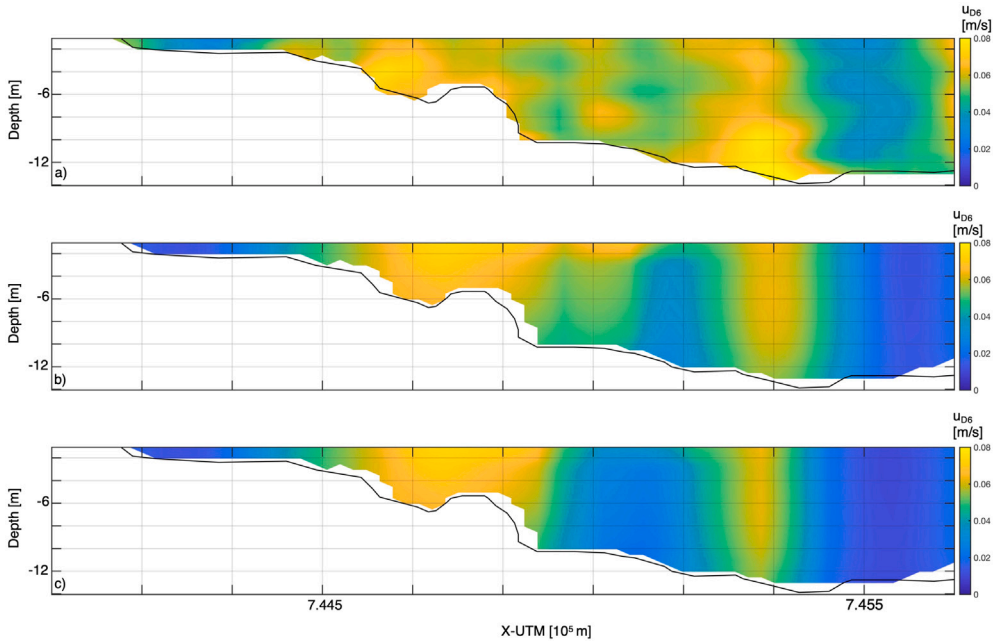

Fig. 10. The D6 band of velocity during spring tide. Panel (a) observed data, panel (b) modeled data, and panel (c) modeled data without including the bridge pile.

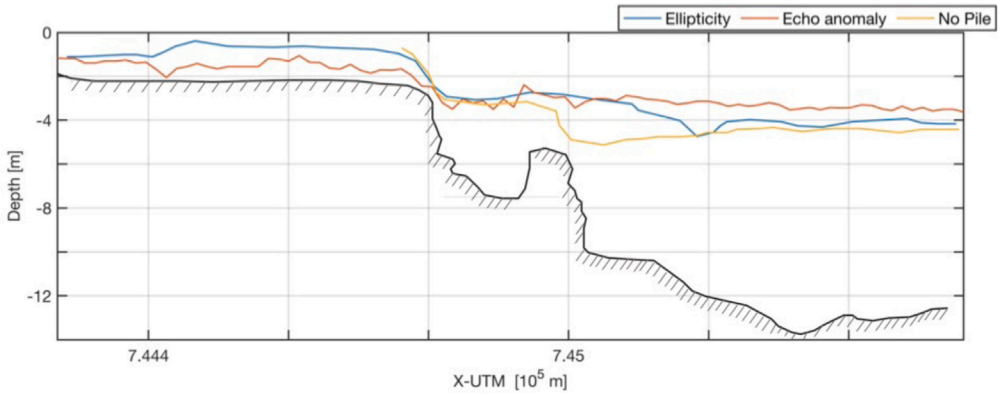

Fig. 11. Location of the pycnocline calculated with the ellipticity (blue), echo anomaly (orange) and numerical model without pile (yellow).

highlight that the pile triggers tidal current amplitude modifications in the D2, D4 and D6 bands, as well as changes in the location of the pycnocline and the sediment transport. Numerical results corroborate these results. The most energetic amplitude (D2) is reduced up to 50% in the area closest to the pile. The pile also amplifies the non-linear terms due to friction both in the area of the pile and its wake (100%). Furthermore, the pile causes a phase lag of 30 min and an increase of sediment transport rates. The greatest changes were observed during tidal flood periods. Therefore, this study reveals that cross-sectional variability of nonlinearities in an altered mesotidal estuary can be affected by bridge pilings, and that this influence is evident in the D6 band. In addition, the influence of these nonlinear terms differs between neap and spring tides.

The semi-minor axis of the semidiurnal tidal currents and the echo intensity of the current profilers indicate that the pycnocline is located at a depth of 4–6 m. Excluding the bridge pile in a numerical simulation, the pycnocline is delimited between 5 and 6 m. The highest sediment transport values are found in the channel and become less relevant close to the pile and its surroundings. Thereby, the amount of sediment transport is reduced because the pile works as an obstacle in flood tides, whereas during ebb tides there is an increase in sediment transport since the pile does not hinder the flow. These conclusions could be extended from studies associated with bridge piles to other constructions such as wind or wave energy farms, which can also interfere with tidal flow structures and sediment transport. Thus, detailed hydrodynamics and environmental studies must be carried out when planning these types of structures in coastal areas where either tides or bathymetric straits are relevant.

CRediT authorship contribution statement

Carmen Zarzuelo: Conceptualization, Methodology, Numerical modeling, Writing – original draft, Software, Data curation, Formal analysis, Investigation. **Alejandro López-Ruiz:** Conceptualization, Writing – original draft, Supervision, Software, Formal analysis, Investigation. **Arnoldo Valle-Levinson:** Investigation, Writing –

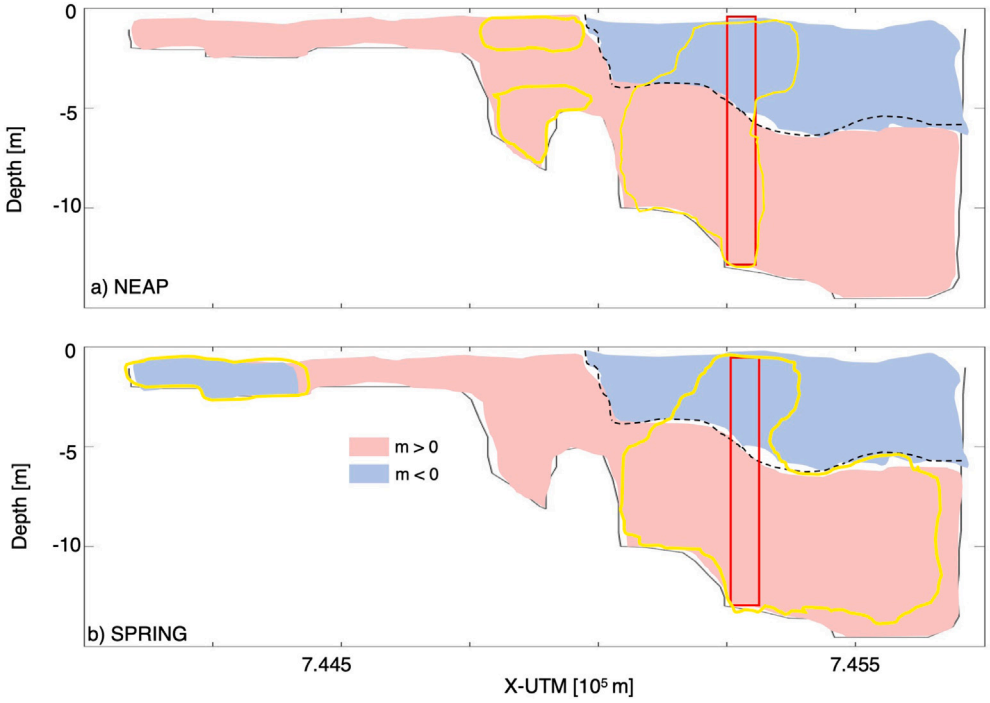

Fig. 12. Sketch of the behavior during neap (a) and spring (b) tides. The dashed line represents the estimated location of the pycnocline from tidal ellipses parameters. Red color corresponds to a clockwise rotation ($m > 0$) and blue color to a counterclockwise rotation (m<0). The yellow line corresponds to the outline of the ebb dominance. The wake of the pile is highlighted in red.

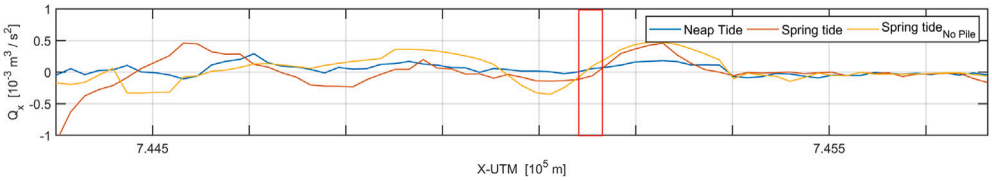

Fig. 13. The along vertically averaged residual sediment transport component influenced by D2, D4 and D6 bands during neap (blue) and spring (orange) tide. Yellow line represents the numerical model results not considering the pile. Red rectangle corresponds to the location of the pile.

original draft. **Manuel Díez-Minguito:** Investigation, Writing – original draft. **Miguel Ortega-Sánchez:** Conceptualization, Writing – original draft, Supervision, Funding acquisition.

Declaration of competing interest

The authors declare that they have no known competing financial interests or personal relationships that could have appeared to influence the work reported in this paper.

Acknowledgments

This work has been supported by the Spanish Ministry of Economy and Competitiveness, Project CTM2017-89531-R (PIRATES) and by Department of Economy, Knowledge, Business and Universities of the Andalusian Regional Government, Spain (Project A-TEP-88-UGR20). One anonymous reviewer is acknowledged for their comments and suggestions which improved significantly the manuscript.

References

Andersen, J.H., Al-Hamdani, Z., Harvey, E.T., Kallenbach, E., Murray, C., Stock, A., 2020. Relative impacts of multiple human stressors in estuaries and coastal waters in the North sea–Baltic sea transition zone. Sci. Total Environ. 704, 135316.

Aubrey, D., Speer, P., 1985. A study of non-linear tidal propagation in shallow inlet/estuarine systems part I: Observations. Estuar. Coast. Shelf Sci. 21 (2), 185–205.

Bagnold, R., 1963. Mechanics of marine sedimentation. Sea 3, 507–528.

Blanton, J.O., Lin, G., Elston, S.A., 2002. Tidal current asymmetry in shallow estuaries and tidal creeks. Cont. Shelf Res. 22 (11–13), 1731–1743.

Cearreta, A., Irabien, M.J., Pascual, A., 2004. Human activities along the Basque coast during the last two centuries: geological perspective of recent anthropogenic impact on the coast and its environmental consequences. In: Oceanography and Marine Environment of the Basque Country. In: Elsevier Oceanography Series, vol. 70, Elsevier Amsterdam, pp. 27–50.

Chen, J., Tang, H.-w., Xiao, Y., Ji, M., 2013. Hydrodynamic characteristics and sediment transport of a tidal river under influence of wading engineering groups. China Ocean Eng. 27 (6), 829–842.

Dastgheib, A., Roelvink, J., Wang, Z., 2008. Long-term process-based morphological modeling of the marsdiep tidal basin. Mar. Geol. 256 (1–4), 90–100.

Dronkers, J., 1986. Tidal asymmetry and estuarine morphology. Netherlands J. Sea Res. 20 (2–3), 117–131.

Egbert, G.D., Erofeeva, S.Y., 2002. Efficient inverse modeling of barotropic ocean tides. J. Atmos. Ocean. Technol. 19 (2), 183–204.

Geyer, W.R., MacCready, P., 2014. The estuarine circulation. Annu. Rev. Fluid Mech. 46, 175–197.

Gross, E.S., MacWilliams, M.L., Kimmerer, W.J., 2009. Three-dimensional modeling of tidal hydrodynamics in the san Francisco Estuary. San Francisco Estuary Watershed Sci. 7 (2).

Guo, J., Ma, C., Ai, B., Xu, X., Huang, W., Zhao, J., 2020. Assessing the effects of the Hong Kong-Zhuhai-Macau bridge on the total suspended solids in the Pearl river estuary based on landsat time series. J. Geophys. Res. : Oceans 125 (8), e2020JC016202.

Hoitink, A., Hoekstra, P., Van Maren, D., 2003. Flow asymmetry associated with astronomical tides: Implications for the residual transport of sediment. J. Geophys. Res. : Oceans 108 (C10).

Lesser, G.R., Roelvink, J.v., van Kester, J.T.M., Stelling, G., 2004. Development and validation of a three-dimensional morphological model. Coast. Eng. 51 (8–9), 883–915.

Lieberthal, B., Huguenard, K., Ross, L., Bears, K., 2019. The generation of overtides in flow around a headland in a low inflow estuary. J. Geophys. Res. : Oceans 124 (2), 955–980.
Miller, J.L., Valle-Levinson, A., 1996. The effect of bridge piles on stratification in lower chesapeake bay. Estuaries 19 (3), 526–539.
Murshid, S., Mariotti, G., 2021. Geometry of natural and engineered tidal inlets. Coast. Eng. 164, 103828.
Pareja-Roman, L.F., Chant, R.J., Sommerfield, C.K., 2020. Impact of historical channel deepening on tidal hydraulics in the Delaware Estuary. J. Geophys. Res. : Oceans 125 (12), e2020JC016256.
Parker, B.B., 1991. The relative importance of the various nonlinear mechanisms in a wide range of tidal interactions. In: Tidal Hydrodynamics. pp. 237–268.
Pawlowicz, R., Beardsley, B., Lentz, S., 2002. Classical tidal harmonic analysis including error estimates in MATLAB using T_TIDE. Comput. Geosci. 28 (8), 929–937.
Qiao, S., Pan, D., He, X., Cui, Q., 2011. Numerical study of the influence of Donghai bridge on sediment transport in the mouth of Hangzhou bay. Procedia Environ. Sci. 10, 408–413.
Rawson, A., Rogers, E., 2015. Assessing the impacts to vessel traffic from offshore wind farms in the Thames Estuary. Zeszyty Naukowe Akademii Morskiej W Szczecinie 43 (115), 99–107.
Ross, L., Pérez-Santos, I., Valle-Levinson, A., Schneider, W., 2014. Semidiurnal internal tides in a patagonian fjord. Prog. Oceanogr. 129, 19–34.
Ross, L., Sottolichio, A., 2016. Subtidal variability of sea level in a macrotidal and convergent estuary. Cont. Shelf Res. 131, 28–41.
Simpson, J., Bos, W., Schirmer, F., Souza, A., Rippeth, T., Jones, S., Hydes, D., 1993. Periodic stratification in the Rhine ROFI in the north-sea. Oceanol. Acta 16 (1), 23–32.
Simpson, J., Souza, A., 1995. Semidiurnal switching of stratification in the region of freshwater influence of the Rhine. J. Geophys. Res. : Oceans 100 (C4), 7037–7044.
Souza, A., Simpson, J., 1996. The modification of tidal ellipses by stratification in the Rhine ROFI. Cont. Shelf Res. 16 (8), 997–1007.
Valle-Levinson, A., 2021. Dynamics-based classification of semienclosed basins. Regional Stud. Mar. Sci. 101866.
Valle-Levinson, A., Castro, A.T.n., De Velasco, G.G., Armas, R.G., 2004. Diurnal vertical motions over a seamount of the southern gulf of california. J. Mar. Syst. 50 (1–2), 61–77.
Wang, X., Frangopol, D.M., Dong, Y., Lei, X., Zhang, Y., 2018. Novel technique for configuration transformation of 3D curved cables of suspension bridges: Application to the Dongtiao river bridge. J. Perform. Constr. Facil. 32 (4), 04018045.
Wei, W., Dai, Z., Mei, X., Liu, J.P., Gao, S., Li, S., 2017. Shoal morphodynamics of the changjiang (Yangtze) estuary: Influences from river damming, estuarine hydraulic engineering and reclamation projects. Mar. Geol. 386, 32–43.
Wu, C.S., Yang, S., Huang, S., Mu, J., 2016. Delta changes in the Pearl river estuary and its response to human activities (1954–2008). Quat. Int. 392, 147–154.
Xie, D.-f., Shu, G., Wang, Z.-b., Pan, C.-h., 2013. Numerical modeling of tidal currents, sediment transport and morphological evolution in Hangzhou Bay, China. Int. J. Sediment Res. 28 (3), 316–328.
Yang, Y., Melville, B.W., Macky, G.H., Shamseldin, A.Y., 2020. Experimental study on local scour at complex bridge pier under combined waves and current. Coast. Eng. 160, 103730.
Zarzuelo, C., Díez-Minguito, M., Ortega-Sánchez, M., López-Ruiz, A., Losada, M.A., 2015. Hydrodynamics response to planned human interventions in a highly altered embayment: The example of the bay of cádiz (Spain). Estuar. Coast. Shelf Sci. 167, 75–85.
Zarzuelo, C., López-Ruiz, A., Díez-Minguito, M., Ortega-Sánchez, M., 2017. Tidal and subtidal hydrodynamics and energetics in a constricted estuary. Estuar. Coast. Shelf Sci. 185, 55–68.
Zarzuelo, C., López-Ruiz, A., Ortega-Sánchez, M., 2019. Evaluating the impact of dredging strategies at tidal inlets: Performance assessment. Sci. Total Environ. 658, 1069–1084.
Zarzuelo, C., López-Ruiz, A., Ortega-Sánchez, M., 2020. Beyond human interventions on complex bays: Effects on water and wave dynamics (Study case Cádiz Bay, Spain). Water 12 (7), 1907.
Zarzuelo, C., López-Ruiz, A., Ortega-Sánchez, M., 2021. The role of waves and heat exchange in the hydrodynamics of multi-basin bays: The example of Cádiz Bay (Southern Spain). J. Geophys. Res. : Oceans 126 (2), e2020JC016346.